Spontaneous Modulation Doping in Semi-Crystalline Conjugated Polymers Leads to High Conductivity at Low Doping Concentration

Aditya Dash, Shubhradip Guchait, Dorothea Scheunemann, Vishnu Vijayakumar, Nicolas Leclerc, Martin Brinkmann, and Martijn Kemerink*

The possibility to control the charge carrier density through doping is one of the defining properties of semiconductors. For organic semiconductors, the doping process is known to come with several problems associated with the dopant compromising the charge carrier mobility by deteriorating the host morphology and/or introducing Coulomb traps. While for inorganic semiconductors these factors can be mitigated through (top-down) modulation doping, this concept has not been employed in organics. Here, this work shows that properly chosen host/dopant combinations can give rise to spontaneous, bottom-up modulation doping, in which the dopants preferentially sit in an amorphous phase, while the actual charge transport occurs predominantly in a crystalline phase with an unaltered microstructure, spatially separating dopants and mobile charges. Combining experiments and numerical simulations, this work shows that this leads to exceptionally high conductivities at relatively low dopant concentrations.

1. Introduction

In recent years, demand for organic semiconductors (OSCs) has boomed due to their potential for low cost fabrication of large-scale optoelectronic applications, and their unsurpassed flexibility, not only in terms of mechanics but also in terms of tunability of properties.[1] Still, enhancing the conductivity remains crucial in optimizing the performance of various devices, ranging from (contact layers in) organic light-emitting diodes (OLEDs)[2] and solar cells,[3] to the active layer in thermoelectrics[4] and sensors,[5] and more. In general, the conductivity of intrinsic OSCs, such as conjugated polymers, is low, but could recently be improved beyond 10^2 S cm^{-1} by introducing mobile charge carriers, primarily by doping.[6–8] However, due to the disordered nature of OSCs, blending with a much higher concentration of dopants ($\approx$1–10 mol %) is needed compared to inorganics where only a few ppm is enough to enhance the conductivity to application-relevant values.

Adding dopants to OSCs comes with several drawbacks, such as significantly deterioration of the microstructure, the mechanical properties as well as the stability of the host material, negatively affecting the conductivity.[9–12] Specifically, for the polythiophenes such as poly(3-hexylthiophene-2,5-diyl) (P3HT) and poly[2,5-bis(3-alkylthiophen-2-yl)thieno[3,2-b]thiophene] (PBTTT), the molecular dopants tend to locate in the side chain layers, disturbing the lamellar packing as well as the $\pi - \pi$ stacking between adjacent polymer backbones within π-stacks. If uncontrolled, such dopant intercalation inside the polymer crystals reduces their degree of crystallinity. Besides the structural degradation, Zuo et al.[13] showed that the dopant ions also limit the charge transport by acting as scattering centers for mobile charge carriers. In strongly disordered (hopping) systems, such as most OSC, the scattering should be understood as strong trapping of the mobile charge carriers in the attractive Coulomb potentials of ionized dopants.[14] Another factor that motivates the efficient use of dopants relates to their toxic and/or aggressive nature as reported for FeCl$_3$ or 2,3,5,6-tetrafluoro-7,7,8,8tetracyanoquinodimethane (F$_4$TCNQ).[15,16] Summarizing, despite several reasons for limiting dopant concentrations in OSC, counteracting factors like a

A. Dash, D. Scheunemann, M. Kemerink
Institute for Molecular Systems Engineering and Advanced Materials
Heidelberg University
Im Neuenheimer Feld 225, 69120 Heidelberg, Germany
E-mail: martijn.kemerink@cam.uni-heidelberg.de
S. Guchait, V. Vijayakumar, M. Brinkmann
Institute Charles Sadron
UPR022
CNRS – Université de Strasbourg
Strasbourg 67034, France
V. Vijayakumar
Department of Chemistry-Ångström
Physical Chemistry
Uppsala University
Uppsala 75120, Sweden
N. Leclerc
Université de Strasbourg
CNRS
ICPEES UMR 7515
Strasbourg F-67087, France

limited doping efficiency and increased scattering, all of which restrict the conductivity, so far necessitate the use of high doping concentrations (> 10 mol%).[17]

In a recent study, Zhong et al.[8] experimentally achieved very high and quickly saturating conductivity when doping oriented P3HT with tris(4-bromophenyl)ammoniumyl hexachloroantimonate (Magic Blue, MB), where the majority of dopants gets preferentially located in the amorphous phase of P3HT. In strong contrast, selective dopant location in the crystalline phase was observed when P3HT[18,19] and PBTTT[20,21] are doped with 1,3,4,5,7,8-hexafluorotetracyanonaphthoquinodimethane (F_6TCNNQ) or F_4TCNQ, resulting in relatively lower and unsaturated conductivity with doping. However, the physical reasons underlying the aforementioned phenomenology are still unknown.

In the community working on inorganic semiconductors, the adverse effects of the insertion of dopants on the charge carrier mobility of the doped material through factors like reduced crystal quality and enhanced impurity scattering are mitigated through so-called modulation doping.[22] Here, the idea is that the dopants are positioned in a wide bandgap layer that is adjacent to a layer of lower bandgap, such that it is energetically favorable for (a fraction of) the mobile counter charges (electrons or holes) to diffuse from the doped region to the low-gap region. The resulting spatial separation between the static ionized dopants and the mobile electrons or holes allows charge carrier mobilities in the plane of the undoped layer in excess of 10^6 cm^2 V^{-1} s^{-1}.[23,24] In the field of organic electronics, we are not aware of any report where this concept is explored for high mobility or conductivity, possibly since the top-down nature of modulation doping runs counter to the low-cost focus of organics. Although stacks of doped and undoped layers are commonly encountered in devices like OLEDs and solar cells, the charge transport in such layers is always perpendicular to the plane of the layers, implying that the current has to pass through the doped layer. A few works have reported the implementation of doped bilayers in organic transistors, but did not demonstrate an improvement in conductivity compared to the case where the low band gap layer is doped directly.[25–27]

Here, we demonstrate that spontaneous or self-organized modulation doping can occur in suitably designed semi-crystalline polymer semiconductor thin films. The required conditions are i) a morphology that contains crystalline and amorphous phases, where the latter should ideally be long-range connected and ii) a dopant that preferentially sits in the amorphous phase. When fulfilled, these conditions give rise to an extremely efficient doping at low doping levels, witnessed by a rapid conductivity increase to exceptionally high values, followed by saturation. We used detailed kinetic Monte Carlo (kMC) simulations to establish the mechanism and identify the various contributing factors. The results match quasi-quantitatively to a range of experiments on systems where dopants are distributed differently over the amorphous and crystalline phases. The occurrence of the required morphologies can be naturally explained by a novel 3-phase model for a drying polymer film. Experimentally, we have so far identified two systems, based on common polymer/dopant combinations, that show spontaneous modulation doping, confirming that the effect is not limited to a specific system but in principle generic.

Table 1. Summary of maximum electrical conductivities and power factors observed upon incremental concentration doping with F_6TCNNQ/acetonitrile and Magic Blue/acetonitrile for P3HT and PBTTT-C_{12}, recorded in the parallel direction to the rubbing.

Dopants	Conductivity [S cm^{-1}]		Seebeck coefficient [µV K^{-1}]		Power Factor [µW mK^{-2}]	
	P3HT	PBTTT-C_{12}	P3HT	PBTTT-C_{12}	P3HT	PBTTT-C_{12}
F_6TCNNQ	520 ± 90	2430 ± 500	45 ± 1	47 ± 1	79 ± 30	530 ± 200
Magic Blue	3460 ± 300	9700 ± 1700	22 ± 1	15 ± 1	170 ± 30	224 ± 39

2. Results and Discussion

In this first section, we present a synoptic view of structural changes and evolution of transport properties induced by doping oriented films of P3HT and PBTTT-C_{12} with two different dopants, namely MB and F_6TCNNQ. **Figure 1** collects the main results obtained for aligned films of P3HT and PBTTT-C_{12} upon doping with F_6TCNNQ and MB, for example, anisotropic charge transport, polarized UV–vis-NIR spectra as well as the variation of the lamellar periodicity d$_{100}$ versus doping concentration as obtained from TEM electron diffraction. The choice of P3HT and PBTTT-C_{12} is justified by the fact that the two OSCs have different and typical morphologies, namely semi-crystalline for P3HT (alternation of amorphous and crystalline domains) and a liquid crystalline phase for PBTTT-C_{12} (see schematic insets in a) and b)). Most results for F_6TCNNQ-doped P3HT and PBTTT-C_{12} are retrieved from the published works of Untilova et al. and Vijakumar et al., respectively whereas the data for MB-doped P3HT are retrieved from the work of Zhong et al.[8,18,28,20] Let us summarize the main findings for these two polymers and two dopants.

As demonstrated previously, MB-doped P3HT displays a very high conductivity up to 3460 ± 300 S cm^{-1} with a saturation at very low solution dopant concentration ([MB] = 0.25 mm L^{-1}). In strong contrast, F_6TCNNQ doping of P3HT results in a lower conductivity of only 520 S cm^{-1} for a higher dopant concentration (Figure 1c and **Table 1**). Polarized UV–vis-NIR spectroscopy (Figure 1e) indicates that both the amorphous and crystalline phases of P3HT are doped by MB as indicated by the presence of the polaronic P1 and P2 bands for light polarization parallel and perpendicular to the chain direction. At the same time, TEM diffraction, (Figure 1g) indicates that the dopants are absent from the crystals of P3HT and hence reside in the amorphous phase.

The same behavior is observed for oriented films of PBTTT-C_{12} (see panels d, f, h). Similarly to P3HT, doping oriented PBTTT-C_{12} films with MB shows a fast saturation to a very high charge conductivity of 9700 ±1700 S cm^{-1} coupled with significant transport anisotropy (Figure S2, Supporting Information) at low dopant concentration ([MB] = 0.6 mm L^{-1}). MB-doping does not induce any sizable modification of the crystal lattice as depicted in Figure S1, Supporting Information. The unit cell parameters d$_{100}$ and d$_{020}$ are almost unaffected by the doping with MB, see Figure 1h. Polarized UV–vis-NIR spectroscopy shows that both the ordered LC and disordered domains of PBTTT-C_{12} are doped by MB. Accordingly, in a similar way as for P3HT, our result demonstrates that SbCl$_6^-$ counterions are not incorporated inside the crystalline domains of PBTTT-C_{12} but are rejected to highly disordered zones of the polymer films.
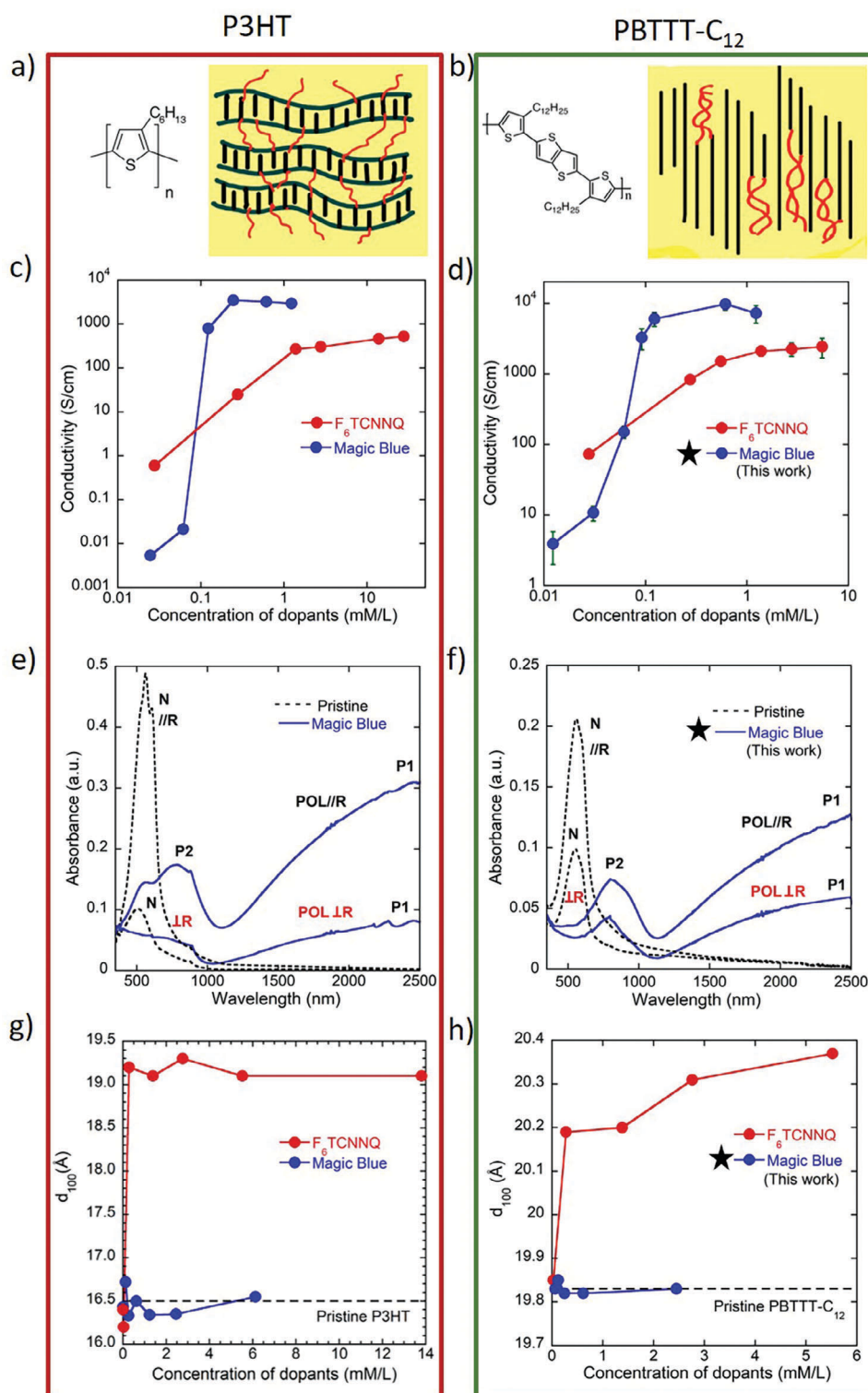
Figure 1. Chemical structure of a) P3HT and b) PBTTT-C_{12} including the a) semi-crystalline lamellar morphology of P3HT and the b) nanomorphology in the liquid crystalline phase of PBTTT-C_{12} (highlighted in the figure).[28] Comparison of the electrical conductivity evolution versus Magic Blue/F_6TCNNQ dopant concentrations in acetonitrile solution measured for oriented c) P3HT and d) PBTTT-C_{12} thin films in the chain direction (rubbing direction).[8,18,20] Recorded UV–vis–NIR spectra for Magic Blue doped oriented e) P3HT (at [MB] = 0.25 mM L^{-1}) and f) PBTTT-C_{12} ([MB] = 0.6 mM L^{-1}) for light polarized parallel (POL//R) and perpendicular (POL⊥R) to the rubbing.[8] Evolution of the lamellar periodicity d_{100} versus dopant concentration (F_6TCNNQ or MB) for oriented g) P3HT and h) PBTTT-C_{12}.[8,18,20] Data collected within this work is highlighted by an asterisk and has been measured using the same material batches and protocols as the corresponding data from literature for P3HT doped with F_6TCNNQ and MB and PBTTT-C_{12} doped with F_6TCNNQ.[8,18,20]

**ADVANCED
SCIENCE NEWS**

www.advancedsciencenews.com

**ADVANCED
MATERIALS**

www.advmat.de

The situation is markedly different when P3HT and PBTTT-C_{12} are doped with F_6TCNNQ. In strong contrast to MB, doping P3HT with F_6TCNNQ results in an important modification to the lattice parameters both along the side chain (d_{100}) and the π-stacking (d_{020}) directions. Untilova et al. measured the conductivity in aligned P3HT films with increasing F_6TCNNQ/acetonitrile dopant concentration and found no clear evidence for saturation even at 10-times higher dopant concentration than MB.[18] A conductivity up to 520 ± 90 S cm^{-1} was obtained in the chain direction at [F_6TCNNQ] = 27.6 mM L^{-1}, see Figure 1c and Table 1. A similar observation was made by Vijayakumar et al. for the oriented liquid crystalline PBTTT-C_{12} polymer.[20] Remarkably, the intercalation of F_6TCNNQ in both P3HT and PBTTT-C_{12} results in similar orientations of the dopants radical anions with their long molecular axis in a plane perpendicular to the polymer backbone (Figure S3, Supporting Information). Polarized UV–vis-NIR spectroscopy also indicates that polaronic bands P1 and P2 are only seen when light is polarized in the chain direction in F_6TCNNQ-doped P3HT and PBTTT-C_{12} films, demonstrating that the disordered domains (amorphous phase) of both polymers are not doped with F_6TCNNQ. There is apparently a clear-cut consequence of the fact that for both polymers only the ordered domains are doped with F_6TCNNQ, namely that the ultimate charge conductivities in F_6TCNNQ-doped films are substantially lower than those observed for MB-doped films. For oriented P3HT (PBTTT-C_{12}) films, the highest conductivity is 3460 S cm^{-1} (9700 S cm^{-1}) for MB and 560 S cm^{-1} (2400 S cm^{-1}) for F_6TCNNQ, as summarized in Table 1.

In contrast to P3HT, the thermoelectric power factor of MB-doped PBTTT-C_{12} lies below that for F_6TCNNQ-doped PBTTT-C_{12} despite the conductivity being significantly higher. The reduced Seebeck coefficient of MB-doped PBTTT-C_{12} may be attributed to the liquid crystalline microstructure of this polymer as compared to the lamellar semi-crystalline structure of P3HT: P3HT has a periodic lamellar structure consisting of crystalline lamellae separated by extended amorphous interlamellar zones, that is, it constitutes a true two-phase system.[28] In contrast, the liquid crystalline structure of PBTTT-C_{12} does not reveal such extended amorphous zones and ordered and disordered domains seem more intermingled. These differences likely affect the typical energy the mobile charges carry upon long-range transport, with the higher and/or more abundant barriers found in P3HT translating in a higher Seebeck coefficient.

The fact that PBTTT-C_{12} systematically shows higher charge conductivities than doped P3HT films must be related to the liquid crystalline structure of the former polymer. As shown in our previous work, high resolution-TEM (HR-TEM) reveals a highly interconnected lattice of crystalline domains in rubbed PBTTT-C_{12} films whereas the periodic semi-crystalline structure of P3HT shows possibly less efficient interconnections between crystalline domains.[28]

Although Figure 1 convincingly demonstrates that the desirable attributes of rapid saturation and high conductivity are not limited to a single "lucky" system, the question about the underlying physics remain enigmatic. In the following, we will argue to establish an explanation by confirming the occurrence of spontaneous modulation doping.

Figure 2a illustrates the concept of spontaneous modulation doping in semi-crystalline conjugated polymers and its effect on mobile charge conduction when dopants locate only in the amorphous phase. Key to the model is the fact that the different microstructures of the two phases creates an offset in the (highest occupied molecular orbital) (HOMO) and lowest unoccupied molecular orbital (LUMO) energy levels (ΔE_{HOMO}), with the more ordered regions having a smaller bandgap, that is, a deeper LUMO and higher HOMO.[29–32] Note that the effective HOMO offset can be affected by differences in energetic disorder too. That is, the density of states (DOS) narrowing and broadening in the ordered and disordered regions, respectively, should generally slightly counteract the HOMO offset, which is accounted for in our simulations.

While this effect of aggregation is well-established in the organic photovoltaics community, it has received surprisingly little attention in terms of more general charge transport. In the current context, the band offset favors the mobile charges to migrate away from the counterions in the amorphous phase, towards the crystalline phase. This charge transfer leads to the formation of an ions-only depletion zone in the amorphous phase and a mobile carriers-only accumulation region at the crystalline-phase side of the interface, see Figure 2b. The resulting space charges give rise to a downward band bending. Consequently, the hole transfer stops when the energy cost associated with overcoming the resulting potential barrier exceeds the energy gain due to the band offset. In other words, this self-limiting phenomenon persists until the Fermi levels in both phases equilibrate. Most importantly, the desired consequence from this phenomenon is the spatial separation of the mobile charges from their counter ions, which suppresses scattering and strong Coulombic trapping[13,14] by the impurity ions. This effect comes on top of the mobility in the crystalline phase anyhow being (expected to be) higher due to the higher degree of order, which is not perturbed by incorporation of dopants. Under the condition that a long-range interconnection of the amorphous and crystalline regions exists, the aforementioned factors lead to a fast increase in conductivity with doping concentration with a pronounced saturation due to the self-limiting charge transfer process.

Apart from the conductivity in the accumulation layer, conduction will, in general, also take place in the bulk of the crystalline and amorphous phases. For later discussions, it is useful to imagine the transport in a generic semi-crystalline material in terms of three parallel resistors, see Figure 2c, where the values of the different resistors depend on the transport properties and the average doping concentration (N_D) as well as the relative distribution over the separate phases (D_A: D_C). Although the parallel resistor model will turn out to be instructive, it must be borne in mind that it formally only holds for long-range interconnected domains. In all other cases, a more complicated combination of series and parallel resistances would be needed.

To confirm whether the mechanism in Figure 2a–c can indeed explain the experimentally observed behavior in Figure 1, we numerically generated approximate morphologies for semi-crystalline materials to serve as input for the kMC transport modeling. In the first approach, we used the cellular automaton model of Peumans and Forrest to generate convoluted two-phase morphologies as shown in Figure 2d.[33] Details of the model are given in the SI, Section 2. Starting from a random mixture, the characteristic feature size is determined by the number of annealing steps. However, generating these morphologies with larger
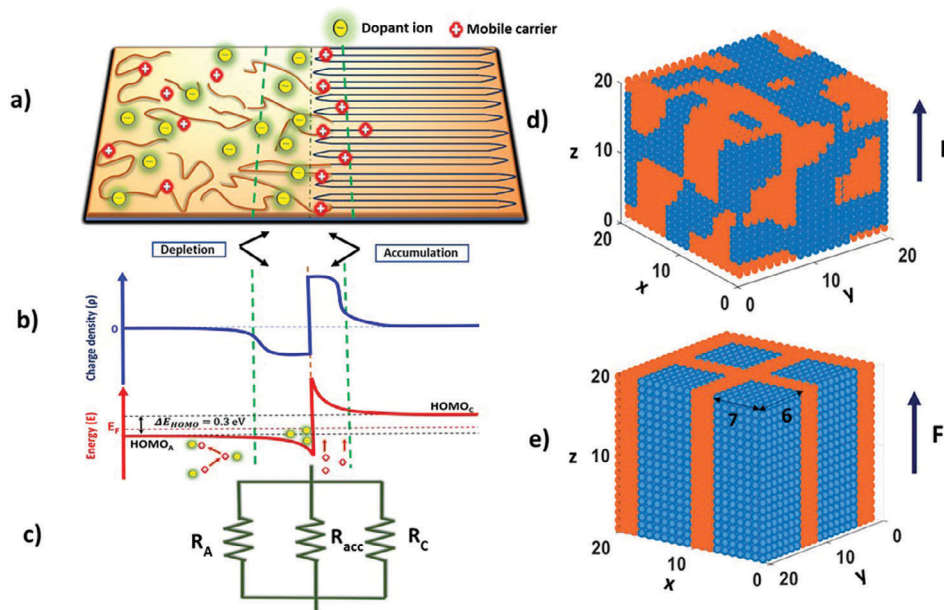
Figure 2. Illustration of the spontaneous modulation doping model. a) Schematic morphology with dopants (yellow) sitting preferentially in the amorphous polymer phase (wiggly lines); near the interface with the ordered polymer phase (zigzag lines), a fraction of mobile charges (red) is transferred to the latter phase, forming a positive accumulation layer, leaving a negative depletion region behind; b) corresponding net charge distribution (blue line) and energy diagram (red line), showing the band bending effect of the negative (ionic) and positive (mobile) charges on the polymer HOMO. The HOMO offset between the two phases is due to the difference in aggregation and concomitantly in wavefunction delocalization, leading to a smaller bandgap in the aggregated phase; c) Parallel resistance model accounting for the conductive channels in the amorphous (A), crystalline (C), and accumulation (acc) layer. d) Morphology obtained by cellular automata model consisting of aggregated (blue) and amorphous (red) phases; e) Corresponding simplified pillar morphology, with the pillars parallel to the rubbing direction. The electric field (F) is applied parallel to the z-axis. Numbers in (d,e) are unit cells with an inter-site distance $a_{NN} = 1.8$ nm.

feature sizes is computationally expensive, so we instead used the stylized pillar morphology illustrated in Figure 2e. Both morphologies yield essentially indistinguishable results when the same feature sizes and material properties are used, as demonstrated in Figure S7a, Supporting Information, with the pillar morphology having the advantage of being more tractable.

The generated morphologies were used as input for kMC simulations for P3HT and PBTTT, accounting for the different ratios of crystalline to amorphous phase volume, as well as for the preferential amorphous and crystalline doping by MB (D_A : D_C = 1: 0) and F_6TCNNQ (D_A : D_C = 0: 1). In **Figure 3a**, the simulated results for both polymer systems demonstrate a quantitatively similar quick increase in conductivity followed by a saturation upon MB doping, which is less pronounced when F_6TCNNQ is added, in agreement with the experimental findings in Figure 1. The energy level offsets between dopant LUMO and polymer HOMO, ΔE_{dope}, are such that integer charge transfer (ICT) occurs.[34,18] The other parameters used in the kMC simulations, as listed in **Table 2**, are set to typical values and can be considered generic.

For preferential dopant incorporation in the amorphous phase (MB), the model shows a negative, hole-depleted region on the amorphous (left) side of the interface, flanked by a positive hole accumulation layer on the crystalline (right) side, see Figure 3b,c. In contrast, for preferential incorporation in the crystalline phase (P3HT:F_6TCNQ), the holes are restricted to the crystalline phase as it is energetically unfavorable to transfer to the amorphous phase, see Figure S8, Supporting Information. Similar spatial

charge potential distributions are obtained for the PBTTT systems. The conductivity saturation for the two MB-doped polymers follows from the dominance of R_{acc} and the amount of charge that can be stored in the accumulation layer that is limited by the band offset ΔE_{HOMO} and the dielectric constant ϵ_r, but not by the doping concentration N_D. The absence of saturation for the F_6TCNNQ-doped material is therefore an indication for the absence of an accumulation layer, and the continuous increase is the consequence of an "unlimited" increase in conductivity of the bulk of the crystalline phase, that is, a continuous decrease of $R_C \propto 1/\mu_C N_D$.[35] The reason that the similar decrease of $R_A \propto 1/\mu_A N_D$ for preferential doping in the amorphous phase does not overwhelm the saturation behavior is that the associated charge carrier mobility μ_A is much lower, such that $R_A \gg R_{\text{acc}}$.

Note that the band bending causes the free charge carrier density in the bulk of the crystalline phase to remain (almost) zero (Figure 3b), such that also R_C remains very large. Since the hole accumulation is limited to a relatively narrow region, the crystalline regions need not be very wide for the modulation doping to fully develop. Figure S11, Supporting Information shows only a weak, ≈10%, conductivity increase upon broadening the crystalline regions from 3 (≈5 nm) to 7 (13 nm) unit cells. HRTEM images of rubbed P3HT films show that the extension of crystalline domains in the chain direction is typically of the order of 14 nm for films rubbed at 220 °C.[36]

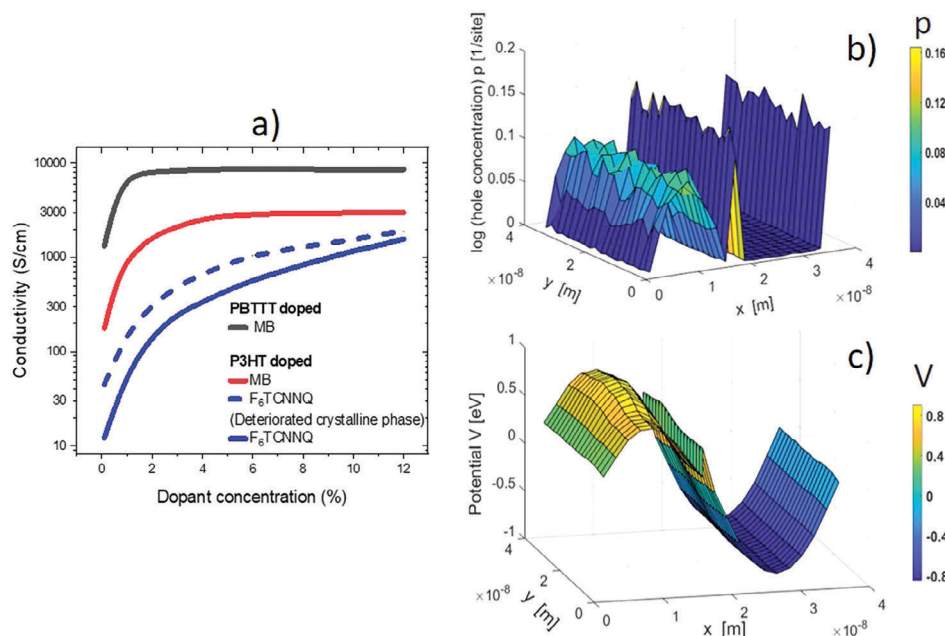To better understand the differences between the red (preferred amorphous) and blue (preferred crystalline) curves in

2311303 (5 of 9)

Figure 3. kMC simulations for a) conductivity versus dopant concentration for P3HT and PBTTT, doped with either MB or F_6TCNNQ, as indicated in the legend; b) the hole concentration and c) electrostatic potential including HOMO level offset for P3HT:MB at 4% dopant concentration. For clarity in panels (b) and (c), the morphologies used consist of rectangular (alternating slabs) inclusions instead of are of the square (pillar) inclusions shown in Figure 2. The square and rectangular morphologies yield similar observables if the feature sizes are similar. Hence, in (b) and (c), the amorphous (crystalline) phase sits at $x < 16.2$ nm ($x > 16.2$ nm). Further model parameters are given in Table 2.

Table 2. Model parameters used in the simulations of Figure 3. A complete description of the model parameters, including how rubbing-induced anisotropy is accounted for, is discussed in Supporting Information, chapter 5.

P3HT		Magic Blue	F6TCNNQ
	Crystalline Inclusion unit cell	$11 \times 20 \times 20$ in a $20 \times 20 \times 20$	
	$\sigma_{dos, A}$ (meV)	75	
	$\sigma_{dos, C}$ / deteriorated phase $\sigma_{dos, C}$ (meV)	45/65	
	$\nu_{0,A}$ (s^{-1})	3.3×10^9	
	$\nu_{0,C}$ (s^{-1})	3.3×10^{11}	
	ΔE_{HOMO} (eV)	0.3	
	D_A:D_C	1:0	0:1
	ΔE_{dope} (eV)	0.3	0.2
	$\sigma_{dos, d}$ (meV)	50	
		Magic Blue	
PBTTT	Crystalline Inclusion unit cell	$23 \times 30 \times 30$ in $30 \times 30 \times 30$	
	$\sigma_{dos, A}$ (meV)	75	
	$\sigma_{dos, C}$ / deteriorated phase $\sigma_{dos, C}$ (meV)	45	
	$\nu_{0,A}$ (s^{-1})	2×10^{10}	
	$\nu_{0,C}$ (s^{-1})	2×10^{12}	
	ΔE_{HOMO} (eV)	0.3	
	D_A:D_C	1:0	
	ΔE_{dope} (eV)	0.3	
	$\sigma_{dos, d}$ (meV)	50	

Figure 3, we must consider the possible factors contributing to the total conductivity. These are i) intrinsic (low carrier density) mobility differences between the two phases, which, in the used Gaussian disorder model (GDM), is a function of the energetic disorder $\sigma_{DOS}^{a/c}$ and the attempt-to-hop rate $\nu_0^{a/c}$; ii) differences in state filling; iii); differences in Coulomb scattering by ionized dopants and iv) differences in spatial confinement (2D versus 3D). Considering the effects in terms of the parallel resistor model Figure 2c, factor (iv) will decrease the conductivity of the interfacial accumulation layer w.r.t. the same density in a bulk phase. However, for the given parameters, the 2D confinement is relatively weak, cf. the discussion at Figure S11, Supporting Information, for which case it was shown that the associated increase in R_{acc} is limited.[37–39] The difference between the red and dashed blue lines, which have equal hopping parameters, thus reflects the combined effects of (ii), state filling, and (iii), Coulomb scattering. The latter is a detrimental effect that is weakest in the modulation doped case while the former is a beneficial factor that is strongest in the high-density accumulation layer. Hence, both factors contribute to the observed conductivity difference, see Figure S10d, Supporting Information for a quantification of the effect of the dielectric constant.

Comparing the differences between the preferential-amorphous and preferential-crystalline cases in the experiment, Figure 1c,d, to the red and dashed blue curves in Figure 3a shows that the effect of spontaneous modulation doping in the experiment in terms of (differences in) steepness of the conductivity versus doping concentration curve $\sigma(N_D)$ is larger than in the simulations and cannot be explained with realistic

**ADVANCED
SCIENCE NEWS**

www.advancedsciencenews.com

**ADVANCED
MATERIALS**

www.advmat.de

dielectric parameters. Hence, the measured effect must be due to an additional factor, most likely an increase in energetic disorder and/or a reduction in attempt-to-hop frequency associated with a reduced molecular packing quality brought about by the incorporation of the dopants – that is, effect (i) above. The solid blue line in Figure 3a is calculated for a modest deterioration of σ_{DOS}^c and ν_0^c, indeed leading to a $\sigma(N_D)$-curve that more closely matches the experiment. A further discussion of the role of the various model parameters can be found in Figures S10–S12, Supporting Information. Summarizing the above, the experimentally observed rapid increase of conductivity with doping concentration can be semi-quantitatively explained as an effect of spontaneous modulation doping, with state filling, reduced scattering and a preserved morphology all contributing to the high absolute conductivity values. These effects would come on top of any differences in doping efficiency or Coulomb interaction that might result from the dopants occupying different positions relative to the conjugated backbone that are not accounted for in the present calculations.[40] Note, however, that the effect calculated in Ref.[40] is unlikely to be able to explain the observed differences between MB and F_6TCNQ doping. As the latter preferentially intercalates in the alkyl chains in the ordered regions, this should correspond to an optimal situation in terms of Ref.[40] and the preferential incorporation of MB in the more random amorphous phase should then lead to a lower doping efficiency and concomitantly a less steep increase in conductivity, opposite to the observations.

To investigate the reason for the preferential doping in the amorphous phase, to further validate the relevance of the assumed morphology and to explicitly investigate the anisotropy due to rubbing, we developed a simplified model for the solidification of a polymer from a drying solution. While full molecular dynamics simulations of drying polymer solutions are notoriously time consuming and all but impossible for rubbed films, our model produces realistic-looking morphologies in a matter of seconds or less on a desktop pc. The model distinguishes three distinct phases in the drying solution: a solidified dry phase, a drying phase, and a dissolved phase. While in reality, the transitions between these phases are gradual and polymer chains always interact with their surroundings, the model is based on the assumption that the final conformation of a polymer chain is mostly determined by intra-chain interactions within the drying chain and by inter-chain interactions with already solidified material; the weaker interactions with dissolved material are neglected.

In an actual drying film, the final morphology is determined by a multitude of factors, including polymer stiffness (bending, torsion), interactions with other polymers (e.g., pi-pi-stacking) and the substrate, and viscous forces associated with the evaporating solvent. In the 3-phase model, these are reduced to 3 intra- and 4 inter-chain interactions that are accounted for through nearest-neighbor interactions that depend on the relative orientation of neighboring monomer pairs, c.f. Figure S5, Supporting Information. All other interactions, including the effects of rubbing, are lumped into homogeneous "alignment fields" that put an energy penalty or bonus on a particular orientation or direction of a monomer. Despite its simplicity, this allows to make, for instance, in-plane aligned films with edge-on orientation as illustrated in Figure S6a–c, Supporting Information, Section 3, where also more details on the model, including the material parameters and the way the enhanced transport along the conjugated backbone and the π-stacking direction are accounted for, can be found.

Figure 4a shows an aligned polymer morphology mimicking the rubbed polymer morphology. The quasi-1D nature is quantified in Figure S6d, Supporting Information. For the used parameters, the fraction of aggregated material is roughly 54% and is visible as the blue regions in panels (b) and (c). Generally, enhancing the alignment field in the model increases the crystalline phase volume and cluster size, in line with the rubbing mechanism in experiments.[18]

Interestingly, in Figure 4c, a significant number of voids can be seen that predominantly sit in the amorphous phase. This suggests a straightforward explanation for the experimentally observed preferential doping of the amorphous phase. However, it does not explain why one dopant does preferentially end up in these voids (MB) and another (F_6TCNNQ) does not. Inspired by the work of Comin et al., we tentatively propose a scenario where void density and stabilization of the diffusing dopant by integer charge transfer both play a role.[40] While the larger void density would lead to a preferential doping of the amorphous phase by "any" fitting dopant, the fact that F_6TCNNQ is not a sufficiently strong dopant to cause ICT in the amorphous phase would lead a preferential incorporation in the crystalline regions where it is stabilized by ICT. As MB can give rise to ICT in both phases, the void density would become the dominant factor. Additionally, the spherical shape of the magic blue dopant as opposed to the rod-like shape of the F_6TCNNQ dopant might lead to additional steric effects that contribute to the ease with which they intercalate between the alkyl chains in a densely packed aggregated phase. Finally, model calculations in which we assume the dopants to selectively locate in the voids of the entangled polymer morphology give rise to similar charge transport behavior as the pillar inclusion and cellular automata models do, provided comparable feature sizes are considered, c.f. Figure S7b, Supporting Information.

3. Conclusions

In summary, we have unveiled the self-organized modulation doping phenomena in two widely utilized semi-crystalline polymer semiconductors, namely P3HT and PBTTT, resulting in remarkably high conductivity and efficient doping. The aforementioned phenomena is made possible in doped semi-crystalline polymers and primarily driven by i) the offset in HOMO levels between the crystalline and amorphous phases and ii) the positioning of the dopant in the amorphous phase, leading to the formation of a high-density accumulation layer at the interface between the two phases.

The kinetic Monte Carlo transport model semi-quantitatively replicates a wide range of experiments in which the observed preferential dopant position is either the amorphous or the crystalline phase. Its charge transport behavior can intuitively be understood in terms of three parallel channels corresponding to the bulk amorphous and crystalline regions and the interfacial accumulation layer. The model confirms that the very high conductivity in magic blue-doped polymers can arise from spontaneous modulation doping, in which state filling, reduced Coulomb scattering and the preservation of the morphology of the
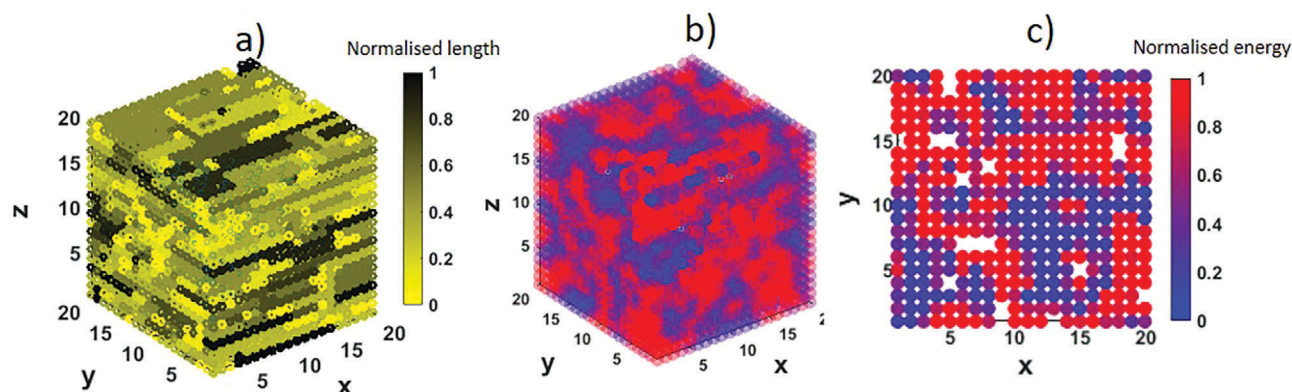
ADVANCED
SCIENCE NEWS
www.advancedsciencenews.com

ADVANCED
MATERIALS
www.advmat.de

Figure 4. a) Three-phase modeled morphology of rubbing-aligned polymers in a periodic box, with longer (black circles) and shorter (yellow circles) polymer chains forming a partially (≈70%) aggregated morphology with a characteristic feature size $r_{typ} = 3.5$ units and an aggregate volume fraction of 0.54. The normalized length 1 and 0 refer to the shortest and longest chains, respectively. b) 3D and c) 2D cross-sectional representation of the total (intra- and inter-chain) interaction energy per monomer of the entangled polymer chains, with blue and red regions indicating energetically stable (aggregated) and unstable (amorphous) phases, respectively. In (c), the white spaces represent voids. Refer to Table S1, Supporting Information for the full set of model parameters. The applied field is along the direction of rubbing, that is, the x-axis.

crystalline (high mobility) phase all contribute to the observed phenomenology. We tentatively attribute the differences in location of preferential incorporation of different dopants to a competition between void density (highest in the amorphous phase) and stabilization of the diffusing dopant by integer charge transfer (stronger for intercalation between the alkyl chains in the crystalline phase). To conclude, spontaneous modulation doping appears a promising design strategy for achieving high conductivity in conjugated polymers at minimal doping levels. It requires a semi-crystalline polymer with long range connected crystalline and amorphous phases, in combination with a sufficiently strong dopant that segregates into the amorphous phase.

Supporting Information

Supporting Information is available from the Wiley Online Library or from the author.

Conflict of Interest

The authors declare no conflict of interest.

Data Availability Statement

The data that support the findings of this study are available from the corresponding author upon reasonable request.

Keywords

doping, morphology, numerical simulation, organic semiconductors

[1] X. Wu, W. Fu, H. Chen, *ACS Appl. Polym. Mater.* **2022**, *4*, 4609.
[2] H. Sasabe, J. Kido, *J. Mater. Chem. C* **2013**, *1*, 1699.
[3] H.-L. Yip, S. K. Hau, N. S. Baek, H. Ma, A. K.-Y. Jen, *Adv. Mater.* **2008**, *20*, 2376.
[4] G. Zuo, H. Abdalla, M. Kemerink, *Adv. Electron. Mater.* **2019**, *5*, 1800821.
[5] D. Yang, D. Ma, *Adv. Opt. Mater.* **2019**, *7*, 1800522.
[6] I. E. Jacobs, Y. Lin, Y. Huang, X. Ren, D. Simatos, C. Chen, D. Tjhe, M. Statz, L. Lai, P. A. Finn, W. G. Neal, G. D'avino, V. Lemaur, S. Fratini, D. Beljonne, J. Strzalka, C. B. Nielsen, S. Barlow, S. R. Marder, I. Mcculloch, H. Sirringhaus, *Adv. Mater.* **2022**, *34*, 2102988.
[7] C. Chen, I. E. Jacobs, K. Kang, Y. Lin, C. Jellett, B. Kang, S. B. Lee, Y. Huang, M. Baloochqarai, R. Ghosh, M. Statz, W. Wood, X. Ren, D. Tjhe, Y. Sun, X. She, Y. Hu, L. Jiang, F. C. Spano, I. Mcculloch, H. Sirringhaus, *Adv. Energy Mater.* **2023**, *13*, 2202797.
[8] Y. Zhong, V. Untilova, D. Muller, S. Guchait, C. Kiefer, L. Herrmann, N. Zimmermann, M. Brosset, T. Heiser, M. Brinkmann, *Adv. Funct. Mater.* **2022**, *32*, 2202075.
[9] S. Zokaei, D. Kim, E. Järsvall, A. M. Fenton, A. R. Weisen, S. Hultmark, P. H. Nguyen, A. M. Matheson, A. Lund, R. Kroon, M. L. Chabinyc, E. D. Gomez, I. Zozoulenko, C. Müller, *Mater. Horiz.* **2022**, *9*, 433.
[10] J. Hynynen, E. Järsvall, R. Kroon, Y. Zhang, S. Barlow, S. R. Marder, M. Kemerink, A. Lund, C. Müller, *ACS Macro Lett.* **2019**, *8*, 70.
[11] J. Moulton, P. Smith, *Synth. Met.* **1991**, *40*, 13.
[12] J. Moulton, P. Smith, *Polymer* **1992**, *33*, 2340.
[13] G. Zuo, H. Abdalla, M. Kemerink, *Phys. Rev. B* **2016**, *93*, 235203.
[14] V. I. Arkhipov, E. V. Emelianova, P. Heremans, H. Bässler, *Phys. Rev. B* **2005**, *72*, 235202.
[15] A. I. Hofmann, R. Kroon, L. Yu, C. Müller, *J. Mater. Chem. C* **2018**, *6*, 6905.
[16] R. P. Trueman, P. G. Finn, M. M. Westwood, A. Dey, R. Palgrave, A. Tabor, J. B. Phillips, B. C. Schroeder, *J. Mater. Chem. C* **2023**, *11*, 6943.
[17] J. Euvrard, A. Revaux, P.-A. Bayle, M. Bardet, D. Vuillaume, A. Kahn, *Org. Electron.* **2018**, *53*, 135.
[18] V. Untilova, H. Zeng, P. Durand, L. Herrmann, N. Leclerc, M. Brinkmann, *Macromolecules* **2021**, *54*, 6073.

[19] S. Guchait, L. Herrmann, K. Kadri, N. Leclerc, F. Tran Van, M. Brinkmann, *ACS Appl Polym Mater* **2023**, *5*, 5676.

[20] V. Vijayakumar, P. Durand, H. Zeng, V. Untilova, L. Herrmann, P. Algayer, N. Leclerc, M. Brinkmann, *J. Mater. Chem. C* **2020**, *8*, 16470.

[21] H. Zeng, P. Durand, S. Guchait, L. Herrmann, C. Kiefer, N. Leclerc, M. Brinkmann, *J. Mater. Chem. C* **2022**, *10*, 15883.

[22] S. M. Sze, K. K. Ng, *Physics of Semiconductor Devices*, John Wiley & Sons, Ltd, Hoboken, **2006**.

[23] Y. J. Chung, C. Wang, S. K. Singh, A. Gupta, K. W. Baldwin, K. W. West, M. Shayegan, L. N. Pfeiffer, R. Winkler, *Phys. Rev. Mater.* **2022**, *6*, 034005.

[24] W. I. Wang, *Appl. Phys. Lett.* **1982**, *41*, 540.

[25] S.-J. Wang, M. Panhans, I. Lashkov, H. Kleemann, F. Caglieris, D. Becker-Koch, J. Vahland, E. Guo, S. Huang, Y. Krupskaya, Y. Vaynzof, B. Büchner, F. Ortmann, K. Leo, *Sci. Adv.* **2022**, *8*, eabl9264.

[26] I. Lashkov, K. Krechan, K. Ortstein, F. Talnack, S.-J. Wang, S. C. B. Mannsfeld, H. Kleemann, K. Leo, *ACS Appl. Mater. Interfaces* **2021**, *13*, 8664.

[27] W. Zhao, Y. Qi, T. Sajoto, S. Barlow, S. R. Marder, A. Kahn, *Appl. Phys. Lett.* **2010**, *97*, 123305.

[28] V. Vijayakumar, Y. Zhong, V. Untilova, M. Bahri, L. Herrmann, L. Biniek, N. Leclerc, M. Brinkmann, *Adv. Energy Mater.* **2019**, *0*, 1900266.

[29] C. Groves, *Energy Environ. Sci.* **2013**, *6*, 1546.

[30] W. C. Tsoi, S. J. Spencer, L. Yang, A. M. Ballantyne, P. G. Nicholson, A. Turnbull, A. G. Shard, C. E. Murphy, D. D. C. Bradley, J. Nelson, J.-S. Kim, *Macromolecules* **2011**, *44*, 2944.

[31] F. Paquin, G. Latini, M. Sakowicz, P.-L. Karsenti, L. Wang, D. Beljonne, N. Stingelin, C. Silva, *Phys. Rev. Lett.* **2011**, *106*, 197401.

[32] D. P. Mcmahon, D. L. Cheung, A. Troisi, *J. Phys. Chem. Lett.* **2011**, *2*, 2737.

[33] P. Peumans, S. Uchida, S. R. Forrest, *Nature* **2003**, *425*, 158.

[34] A. Hamidi-Sakr, L. Biniek, J.-L. Bantignies, D. Maurin, L. Herrmann, N. Leclerc, P. Lévêque, V. Vijayakumar, N. Zimmermann, M. Brinkmann, *Adv. Funct. Mater.* **2017**, *27*, 1700173.

[35] A. Dash, D. Scheunemann, M. Kemerink, *Phys. Rev. Appl.* **2022**, *18*, 064022.

[36] A. Hamidi-Sakr, L. Biniek, S. Fall, M. Brinkmann, *Adv. Funct. Mater.* **2016**, *26*, 408.

[37] A. Sharma, F. W. A. Van Oost, M. Kemerink, P. A. Bobbert, *Phys. Rev. B* **2012**, *85*, 235302.

[38] A. Sharma, N. M. A. Janssen, S. G. J. Mathijssen, D. M. De Leeuw, M. Kemerink, P. A. Bobbert, *Phys. Rev. B* **2011**, *83*, 125310.

[39] H. Abdalla, S. Fabiano, M. Kemerink, *Phys. Rev. B* **2017**, *95*, 085301.

[40] M. Comin, V. Lemaur, A. Giunchi, D. Beljonne, X. Blase, G. D'avino, *J. Mater. Chem. C* **2022**, *10*, 13815.